The Impact of Advanced Airfoils on Rotor Hover Performance

Tin-Chee Wong[1]
US Army Research Development and Engineering Command, Redstone Arsenal, AL, 35898

Unsteady, compressible Reynolds-averaged Navier-Stokes equation based on an unstructured-grid approach with the Spalart-Allmaras one-equation turbulence model has been used to investigate flow over stationary and oscillating airfoils. The dynamic stall characteristics of Boeing VR-7 airfoils with and without slats were computed and compared with experimental data. Tunnel walls were included in the simulation to investigate the blockage effect on the aerodynamic characteristics. The computed dynamic stall characteristics correlate well with experimental data. In general, the results of airfoil with slat show improvement in the lift characteristics and suppress the negative pitching moment in all dynamic cases. Furthermore, a helicopter hover performance code is used to quantify performance gains using the computed static characteristics of the advanced airfoils. The addition of VR-7 with half size slat airfoil to the baseline rotor blade shows a hover performance gain.

Nomenclature

α	=	angle of attack
Cl_{max}	=	maximum static lift coefficient
C_P	=	power coefficient or pressure coefficient
Cp	=	pressure coefficient
C_p	=	measured power coefficient
C_T	=	thrust coefficient
c	=	chord
t	=	time step
FM	=	figure of merit
k	=	reduced frequency
M	=	Mach number
P	=	power required
R	=	rotor radius
Re	=	Reynolds number
T	=	rotor thrust
V_{tip}	=	rotor tip speed
y^+	=	non-dimensional wall distance

I. Introduction

The dynamic stall phenomenon has been known to be a major factor that limits helicopter rotor performance at high speed forward flight, in high gravitational force ("g") maneuvers, and at high density-altitude because of the onset of large airloads and vibrations on the blades. Stall occurs on a helicopter rotor at relatively high airspeeds as the advancing and retreating blades begin to operate close to the attached flow limits. In this regard, the advancing blade operates at low angles of attack but close to its shock-induced separation boundary. The retreating blade operates at much lower Mach numbers but encounters very high angles of attack close to stall. These limits are a direct result of the blade flapping and large pitching moments that characterize the performance of an airfoil operating through dynamic stall. Recent desert and mountainous region operations have challenged current helicopters with the requirement to operate effectively in high density-altitude conditions. This need can be partly addressed by the development of main rotors that will allow larger payload capability, higher forward flight speeds, increased range and endurance, and greater maneuverability and agility. Relieving the limitation due to dynamic pitching moment stall through the use of an advanced airfoil such as VR-12, a control nose-droop concept[1] or a passive control device by means of a miniature button shaped leading edge vortex generator[2] may provide useful

[1] Aerospace Engineer, Aeromechanics Division, Aviation Engineering Directorate, AMSRD-AMR-AE-A.

increased rotor limits. Recent work done by the author[3] et al. sought a low-cost method to alleviate dynamic stall using an adjoint optimization technique[4-5] to change the upper surface of the airfoil to have better static characteristics and enable alleviation of the dynamic pitching moment divergence. The resulting modification provides significant pitch link load reduction based on first generation comprehensive analysis code (C81) calculation. The computed results of the modified VR-7 airfoil do not reduce moment divergence at Mach number of 0.4. A recent airfoil design method developed by Martin[6] et al. for heavy lift helicopter used a multi-point design optimization method coupled with a conformal mapping technique to demonstrate a performance gain. Dynamic stall characteristics of these new design airfoils were not documented in the report. Most single-element advanced airfoils are finely tuned shapes that produce high lift while maintaining acceptable pitching moment and drag levels. Further dramatic improvements in the lift characteristics of single-element rotor airfoils are unlikely. Thus, unconventional airfoils technology must be evaluated. It is known from literatures and fixed wing application that lift of an airfoil at high angles of attack can be enhanced by segmenting an airfoil into multiple elements. Moreover, the slat relieves the adverse pressure gradient on the nose of the main element to delay separation, and also eliminate the development of a dynamic-stall vortex during unsteady motions. The objective of this study is to attempt to exploit the static and dynamic aerodynamic benefit associated with different advanced airfoil sections and airfoils with leading edge slats to improve hover performance of a previously studied rotor system.

II. Numerical Algorithm

The unstructured mesh flow solver used in this study is FUN3D. This flow solver has been developed and supported by the NASA Langley Research Center. The governing equations are the three-dimensional, unsteady, compressible Reynolds-averaged Navier-Stokes equations. Details of the numerical algorithm can be found in the literature[7-8]. The code uses an implicit, upwind, finite-volume discretization in which the dependent variables are stored as mesh vertices. Inviscid fluxes at cell interfaces are computed using the flux-differencing scheme of Roe[9] and viscous fluxes are evaluated by using an approach equivalent to a central-difference Galerkin procedure. For steady-state flows, temporal discretization is performed by using a backward Euler time-stepping scheme. At each time step, the linear system of equations is approximately solved with an implicit line relaxation scheme[8]. A local time-step technique is employed to accelerate convergence to steady-state solution. For the time-accurate pitching oscillation, a generalized backward difference scheme (BDF) is used to construct a higher order temporal scheme by extending the difference stencil in time[10]. A temporal error control method is implemented as an exit criterion for the sub-iterative loop of the dual time stepping process. The details of the mesh movement, BDF and temporal error control schemes were documented in reference 8. For all unsteady pitching cases presented in this paper, the solution is second order accurate in time and space and the specified fraction of temporal error control is 0.1. The flow is assumed to be fully turbulent. The one-equation model of Spalart and Allmaras is used for the second closure and solved in a loosely coupled fashion.

In order to evaluate the effects on the rotor performance due to change in airfoil sections of a blade, a hover analysis was conducted using the Lifting Surface Aerodynamics and Performance Analysis of Rotors in Axial Flight (LSAF) hover analysis code.[11-14] LSAF is based on a circulation-coupled prescribed wake to calculate the velocity field within the rotor wake in order to determine the induced velocity at the rotor blade. LSAF uses a lifting surface method to calculate the chordwise and spanwise lift distribution generated by a rotor. A strip-analysis combined with an airfoil table look-up is used to determine the aerodynamic drag. LSAF has been shown to accurately predict the hover performance over a wide range of conditions and thrust levels for a variety of isolated rotors and rotorcraft[14]. The figure of merit or *FM* coefficient is used as a gauge for how efficient a hovering rotor is in terms of thrust for a given power. Figure of merit, power, and thrust coefficient are defined as

$$FM = \frac{C_T^{3/2}}{\sqrt{2}C_P}\ ,\quad C_P = \frac{P}{\rho\pi R^2 V_{tip}^3}\ ,\quad C_T = \frac{T}{\rho\pi R^2 V_{tip}^2}$$

where P and T are power required and thrust of a rotor, respectively. ρ is density, R is radius of a rotor and V_{tip} is the tip speed of a rotor.

III. Results

All meshes used in this study were generated using the Advancing-Front/Local-Reconnection (AFLR) unstructured grid generator developed by Mississippi State University[15]. The meshing strategies, requirements of

grid-density and time-step for unsteady calculations will remain the same as reported in reference 3. The airfoils used for this study were VR-7, VR-7m (from reference 3), VR-7 with slat[16] and four advanced rotorcraft airfoils: RC(4)-10, RC(5)-10, and RC(6)-08 with and without a leading-edge slat. The performance of the RC(4)-10 and RC(6)-08 and RC(6)-08 with slat airfoils were documented in references 17-18. Due to page limitation, only significant results of the current work will be presented in this paper. The airfoil sections of the VR-7, the modified VR-7 (VR-7m) and VR-7 with full size leading-edge slat (Slats0-VR-7) are shown in Figure 1. Figure 2 shows a typical unstructured mesh of a VR-7 airfoil with leading-edge slat. The extent of the computational boundary is 20 chords (c) away from the center of the airfoil and the off-surface spacing is 10^{-6}c yielding a y^+ of one. Meshes used in this study contain at least 350,000 nodes with 1201 points around airfoil and 201 points distributed over the outer boundary. All dynamic stall cases were started with a converged steady-state solution at the corresponding flow conditions, and solutions became periodic at the fourth cycle with 2000 time steps per cycle. For each complete cycle, it requires 89 CPU hours with 32 processors and 174 CPU hours with 24 processors on an SGI Altix Linux and Origin 3900 machines, respectively. All static calculations were started from the corresponding freestream conditions. Steady-state solutions were obtained within 2000 pseudo-time stepping cycle.

A. Unsteady Validation Cases

Two unsteady pitching cases of the VR-7 airfoil section were chosen to represent the tunnel test[19] cases of frames 45117 and 47022. The purpose was to validate the computational mesh, numerical scheme, and the tunnel wall effects. The airfoil was pitched in a sinusoidal motion about the quarter chord, given by the equation

$$\alpha = \alpha_m + \alpha_o \sin(2kM_\infty t)$$

where α is the instantaneous angle of attack, α_m is the mean angle of attack, α_o is the pitch amplitude and k is the reduced frequency. The first dynamic stall case which corresponds to Data Set 45117, has a freestream Mach number (M_∞) of 0.301 and Reynolds number (Re) of 4 million (based on the chord of the airfoil). The sinusoidal motion is defined by the parameter set α_m = 10°, α_o = 10° and k =0.1. Figure 3 shows the comparison of lift, drag and pitching moment coefficients of VR-7 airfoil with (red) and without (green) tunnel walls modeled in the computation and experimental data. The computed aerodynamic coefficients with walls modeled (red) correlate very well with the test data[19] (black). Both results show a large nose-down pitching moment (Figure 3c) and a corresponding drag rise (Figure 3b), which indicates the formation of a shedding vortex from the leading edge and rapid convection downstream. The inclusion of the wind tunnel walls significantly improves the computed lift-curve slope at the upstroke oscillation which was consistent with results reported in reference 20. Snapshots of computed surface-pressure coefficients (Cp) compared with experimental data during unsteady oscillations are shown in Figure 4. The Cp plots of α =18.77˚, 19.81˚ and α =19.80˚, 9.8˚ represent airfoil at the upstroke and downstroke of an oscillating cycle, respectively. Pressure-coefficient plot at α =18.7˚corresponds to the first peak while 19.81° indicates the second peak at the lift curve of Figure 3a. Figure 5 shows side-by-side pressure-coefficient contours of results with (left) and without walls (right) modeled in the computation. The first peak (α =18.76˚) represents the first shedding of stall vortex. As the angle of attack increases to 19.81˚, and the shed vortex travels on the upper surface of the airfoil, it acts to enhance the lift being produced. This gain is shown by the suction peak at α =19.81˚of Figure 4. The corresponding Cp contour plots is shown Figure 5 at α=19.82˚. The Cp plots at α =19.8˚, and α =9.8˚ show good comparison with test data as the airfoil in downstroke of the cycle. Both results show the surface pressure coefficients are under-predicted at α =9.8˚, especially the suction peak close to the leading-edge, which corresponds to the under-prediction of the lift coefficient at the downstroke path. The computed results without tunnel walls show delay in stall prediction. The predicted pressure coefficients indicate a stronger vortex as compared with the experimental data. The discrepancies may be attributed to the time averaging process of the experimental data since there is a slight fluctuation from cycle to cycle. In general, even the computed results without tunnel walls show qualitative agreement with the experimental data.

The second deep stall cases with a freestream Mach number of 0.3, Reynolds number of 4 million with the pitching parameters set to α_m = 15°, α_o = 10° and k =0.051, were computed with and without tunnel walls. The comparison of hysteresis of computed lift, drag and pitching moment coefficients with experimental Data Set 47022 is shown in Figure 6. The results with tunnel walls modeled in the computation show better agreement with the experimental data set in terms of lift slope and stall angle. The experimental data does not have double peaks at the lift curve as compared with computed results. The aerodynamic coefficients indicate double stall characteristics shown in lift and pitching moment coefficients. Since the reduced frequency is half that of the previous case, the air particles have enough time to response to the disturbance from pitching oscillations. The comparison of computed

surface pressure coefficients with experimental data as the airfoil undergoes pitching-up oscillations is shown in Figure 7. The predicted Cp's with tunnel walls modeled in the grid show very good agreement with test data. The Cp plots at angle of attack of 17.98˚ and 19.35˚ correspond to the first and second peak at the lift curve of Figure 6a. As α reaches 20.76˚, the lift coefficient drops to 0.9 and recovers back to value of 1.4 at α =21.73˚. A similar trend has been observed, results even with tunnel walls modeled delay stall prediction. It may be due to the one-equation turbulence model not being adequate for this highly separated vortex flow. Computed pressure drag and moment coefficients over-predicted the peak values of the experimental data. Figure 8 shows the corresponding pressure contours of VR-7 airfoil with wall modeled at the closest values of angle of attack.

The first validation cases of sinusoidal pitched airfoil previously presented was re-computed using three VR-7 airfoils with one-third, half, and full size leading-edge slat at a Mach number of 0.301 with k=0.1. The purpose is to investigate the impact of dynamic stall characteristics due to slat configuration. Since results without tunnel walls modeled in the mesh show qualitative good comparison, tunnel walls were not modeled in this study. The aerodynamic dynamic characteristics of VR-7, VR-7 with full-size slat (Slats0-VR-7), with half-size slat (Slats05-VR-7), and one-third size slat (Slats03-VR-7) configurations is shown in Figure 9. Three airfoils with leading slats suppress dynamic stall at this condition. Both scaled size slat airfoils maintain the same level of lift, lift-curve slope and small pitching moment coefficient, while the full-size slat experiences a nose-up moment during the oscillation cycle. Figure 10 shows the side-by-side comparison of pressure-contour plots for VR-7 with and without half size slat at α =19.82 during the upstroke motion. The leading-edge slat configuration suppresses the formation of dynamic stall vortex.

The double stall validation case also re-computed with VR-7 airfoils with the same leading-edge slat at Mach number of 0.3 and k=0.051. The unsteady aerodynamic coefficients for the last cycle presented in Figure 11 indicates VR-7 airfoil with leading edge slat suppress dynamic stall even at α_m = 15˚. The full-size slat airfoil shows an advantage over those smaller size slat airfoils at high angle of attack regions in terms of lift, and drag while the half size slat maintains close to zero pitching moment for the whole pitching cycle. Pressure-coefficient contours of the half size slat VR-7 airfoil are compared with the baseline VR-7 airfoil at 18.05˚ and 21.76˚ as shown in Figure 12. No stall vortex is observed from the results of half size slat airfoil.

Based on the previous study reported in reference 3, sinusoidal pitched VR-7m airfoil computed at Mach number of 0.4 and Reynolds number of 5 million did not alleviate the stall moment divergence. The same case was re-computed using VR-7 airfoils with three different size leading slat configurations. The computed hysteresis of lift, drag and pitching moment coefficients was shown in Figure 13. Both full- and half-size slat airfoils suppress the dynamic stall at Mach number of 0.4 while the one-third size slat airfoil slightly alleviates the nose-down moment divergence. Previous work reported in reference 3, a minor upper surface modification on the upper surface of the VR-7 airfoil results in reduced in dynamic stall effects for drag and pitching moment with favorable lift overshoot. Pitch-link load was significant reduced based on C81 calculation using the VR-7/VR7m airfoils. Similarly, the modified rotors with the slatted airfoil which has no dynamic stall characteristics may potentially reduce rotor loads at forward flight conditions.

B. Static Slat Airfoils Aerodynamic Characteristics

Helicopter hover performance codes, such as LSAF, utilize look-up tables to provide two dimensional aerodynamic characteristics. In order to investigate the impact of hover performance gain using slatted airfoils, three airfoil tables of VR-7 with full, half and one-third size slat airfoils were generated with the same meshes. The two-dimensional version of FUN3D solver was used to compute static aerodynamic coefficients for VR-7 with leading-edge slat airfoil to construct airfoil tables used for hover performance analysis. The lift, drag and pitching moment coefficients were computed for seven Mach numbers and ninety-eight angles of attack ranging from -180˚ to 180˚. The increment of 5˚ was used everywhere except in the range between -5˚ and 25˚ where 1˚ was used. The generation of each table required 675 CPU hours with 16 processors on a SGI Origin 3900 computer. Figure 14a presents comparison of lift coefficients of VR-7 and three different sizes slat airfoils at Mach number of 0.3. All slat airfoils show maximum lift (Cl_{max}) gain and delay in static stall. The half-size slat airfoil has the most significant benefit with delay in static stall of 6˚ with increasing Cl_{max} of 20% as compared with the baseline VR-7 airfoil. The slight drag penalty associated with the lift benefit is shown in the drag polar of Figure 14b.

C. Hover Performance

In order to evaluate the slatted VR-7 airfoil on hover performance, hover analyses were conducted using the LSAF to compare performance of the blades with the slatted airfoils with the baseline blades. Computations were made for an isolated three-bladed CH-47D rotor using LSAF and compared with the whirl tower test data[21] as a validation case. The baseline blade[21] consists of VR-7 and VR-8 airfoil sections for in-board and tip regions of the blade,

respectively. The VR-7 was extended to 85 percent and then transitioned to become the VR-8 at the tip. Figure 15 shows a plot of Figure of Merit versus with thrust coefficient for an isolated CH-47D rotor using computed airfoil tables. The overall LSAF prediction using computed VR-7/VR-8 airfoil tables shows very good agreement with the whirl tower test data. A series of LSAF computations were performed by changing the VR-7 airfoil section with VR7m, and different slatted airfoil tables over the in-board region, while the tip section remains unchanged. The comparison of computed *FM* between baseline and modified rotors with VR-7m airfoil section up to 30%, 50% and 70% of blade radius is shown in Figure 16. LASF predictions show the blade with VR-7m airfoil section (orange) up to 70% shows hover performance gains beyond C_T values of 0.012. It is an averaged of 0.6 count increase in FM. However, the predicted hover performance of rotor using half-size slat VR-7 and VR-7m combination shows the reversed effect on performance when increasing the extent of the modified airfoil sections (Figure 17). This may be attributed to the drag penalty associated with the lift gain of the half-size slatted airfoil shown in Figure 14b. Figure 17a indicates that hover performance remains the same with addition of a half size slat to VR-7 airfoil section up to 30%*R* while the rest of the blade remains unchanged. Figure 17b implies that there is hover performance gain of 0.6 count with C_T beyond 0.012 with slight sacrifice of 0.05 count decrease in *FM* when replacing VR-7 airfoil section with VR-7m airfoil in addition to adding a half size slat to the baseline rotor.

IV. Conclusion

An unstructured-grid flow solver for the unsteady, compressible Reynolds-averaged Navier-Stokes equations was used to analyze flow over oscillating and stationary airfoils. The dynamic stall characteristics of the VR-7 and three different sizes of slat airfoils were computed for two reduced frequencies and compared with tunnel test data. The airfoil tables of baseline VR-7 and different size slat airfoils were also created and used as inputs for a hover performance code. The hover performance of the CH-47D isolated rotor with the baseline VR-7 airfoil was computed and correlated with whirl tower test data. The following conclusions were drawn from the study:

1. The computational method used in the current study was shown to capture qualitatively deep stall characteristics.
2. When the effects of tunnel walls were modeled in the computation the predicted stall angle and lift-curve slope were agreed more closely with experimental data.
3. The size of the slatted airfoil plays a significant role in suppressing the formation of a dynamic stall vortex and reducing the pitching moment divergence.
4. The addition of a slat to the blade of an isolated rotor can improve hover performance and has the potential to reduce rotor loads in forward flights.
5. In future studies, there is a need to optimize the size and location of the slat addition to the blade using a three-dimensional adjoint design optimization method and investigate the impact of these slat airfoils in forward flight.

Acknowledgments

T-C Wong thanks Drs. Eric Nielsen and Robert Biedron of the NASA Langley Research Center for providing technical support of the FUN2D/3D flow solver. The provision of leading-edge slat geometry by Dr. Chee Tung and test data by Drs. Jim McCroskey, Larry Carr and Mr. Ken W. McAlister of the Aeroflightdynamics Directorate of U. S Army, is greatly appreciated. Last, but not the least, my sincere thanks are due to Mr. Jim A. O'Malley III for sharing his experiences using LSAF and many fruitful discussions. The computer resources of the Department of Defense Major Shared Resource Center and Distributed Center of the Space and Missile Defense Future Warfare Center are gratefully acknowledged.

References

[1]Martin, P. B., McAlister, K. W., Chandrasenkhara, M. S., and Geissler, W., "Dynamic Stall Measurements and Computations for a VR-12 Airfoil with a Variable Droop Leading Edge," 59th American Helicopter Society Annual Forum, Phoenix, Arizona, May 2003.

[2] Geissler, W., Diztz, G., and Mai, H., "Dynamic Stall and Its Passive Control Investigations on the OA209 Airfoil Section," 31st European Rotorcraft Forum, Firenze, Italy Sept. 2005.

[3] Wong, T.-C., O'Malley, III, J. A., and O'Brien, Jr., "Investigation of Effect of Dynamic Stall and Its Alleviation on Helicopter Performance and Loads," 62nd American Helicopter Society Annual Forum, Phoenix, Arizona, May 2006.

[4] Nielsen, E. J., and Anderson, A. K., "Aerodynamic Design Optimization on Unstructured Meshes Using the Navier-Stokes Equations," AIAA Paper 97-4809, 1997.

[5] Nielsen, E. J., Lu, J., Park, M. A., and Darmofal, D. L., "An Implicit Exact Dual Adjoint Solution Method for Turbulent Flows on Unstructured Grids," Computers and Fluids, Vol. 33, No. 9, pp. 1131-1155, November 2004.

[6] Martin, P. B., Rhee, M., Maughmer, M. D., and Somers, D. M., "Airfoil Design and Testing for High-Lift Rotorcraft Applications," American Helicopter Society Specialist's Conference on Aeromechanics, San Francisco, California, Jan. 2008.

[7] Anderson, W. K., and Bonhaus, D. L., "An Implicit Upwind Algorithm for Computing Turbulent Flows on Unstructured Grids," *Computers and Fluids*, Vol. 23, No. 1. pp. 1-21, 1994.

[8] Biedron, R. T., Vatsa, V. N., and Atkins, H. L., "Simulation of Unsteady Flows Using an Unstructured Navier-Stokes Solver on Moving and Stationary Grids," AIAA Paper 2005-5093, June 2005.

[9] Roe, P. L., "Approximate Riemann Solvers, Parameter Vectors, and Difference Schemes," *Journal of Computational Physics,* Vol. 43, No. 2, pp. 357-372, 1981.

[10] Vatsa, V. N. and Carpenter, M. H., "Higher Order Temporal Schemes with Error Controllers for Unsteady Navier-Stokes Equations," AIAA Paper 2005-5245, 2005.

[11] LSAF, Lifting Surface Aerodynamics and Performance Analysis of Rotors in Axial Flight, Software Package, Ver. 2, Computational Methodology Associates, Colleyville, TX. 2003.

[12] Kocurek, J. D., Berkowitz, L. F., and Harris, F. D., "Hover Performance Methodology at Bell Helicopter Textron," Preprint No. 80-3, *36th Annual Forum Proceedings*, American Helicopter Society, Washington, D. C., 1980.

[13] Kocurek, J. D., "A Lifting Surface Performance Analysis with Wake Circulation Coupled Wake for Advanced Configuration Hovering Rotors," Ph.D. Dissertation, Dept. of Aerospace Engineering, Texas A&M University, College Station, TX, 1978.

[14] Kocurek, J. D., and Tangler, J. L., "A Prescribed Wake Lifting Surface Hover Performance Analysis," *Journal of the American Helicopter Society*, Vol. 22, No. 1, pp. 24-35, 1977.

[15] Marcum, D. L., "Generation of Unstructured Grids for Viscous Flow Applications," AIAA Paper 95-0212, 1995.

[16] McAlister, K. and Tung, C., "Suppression of Dynamic Stall with a Leading-Edge Slat on a VR-7 Airfoil," ATCOM Technical Report 92-A-013 or NASA TP 3357, March 1993.

[17] Noonan, K. W., "Aerodynamic Characteristics of Two Rotorcraft Airfoils Designed for Application to the Inboard Region of a Main Rotor Blade," AVSCOM Technical Report 90-B-005 or NASA TP 3009, July 1990.

[18] Noonan K. W., "Aerodynamic Characteristics of a Rotorcraft Airfoil Designed for the Tip Region of a Main Rotor Blade," AVSCOM Technical Report 91-B-003 or NASA TM 4264, May 1991.

[19] McAlister, K. W., Pucci, S. L., McCrosky, W. J., and Carr, L. W., "An Experimental Study of Dynamic Stall on Advanced Airfoil Sections Volume. Pressure and Force Data," USAAVRADCOM TR-82-A-8 (or NASA TM 84245), Sept. 1982.

[20] Duraisamy, K., McCroskey, W. J., and Baeder, J. D., "Analysis of Wind Tunnel Wall Interference Effects on Unsteady Subsonic Airfoil Flows," AIAA Paper 2006-2993, June 2006.

[21] McVeigh, M. A. and McHugh F. J. "Recent Advances in Rotor Technology at Boeing Vertol," 38th Annual Forum of the American Helicopter Society, Anaheim, CA, May 1982.

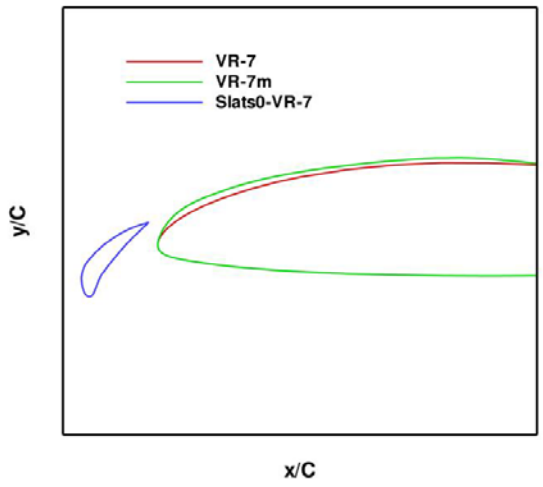

Figure 1 Profiles of baseline VR-7, modified VR-7 and VR-7 with leading-edge slat airfoils.

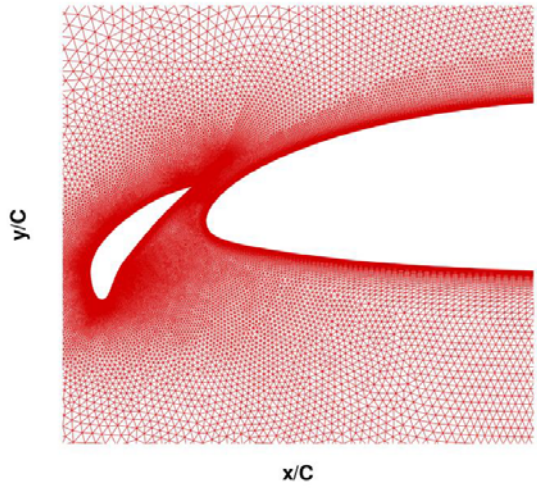

Figure 2 Two-dimensional mesh for the close up of Slats0-VR-7 airfoil.

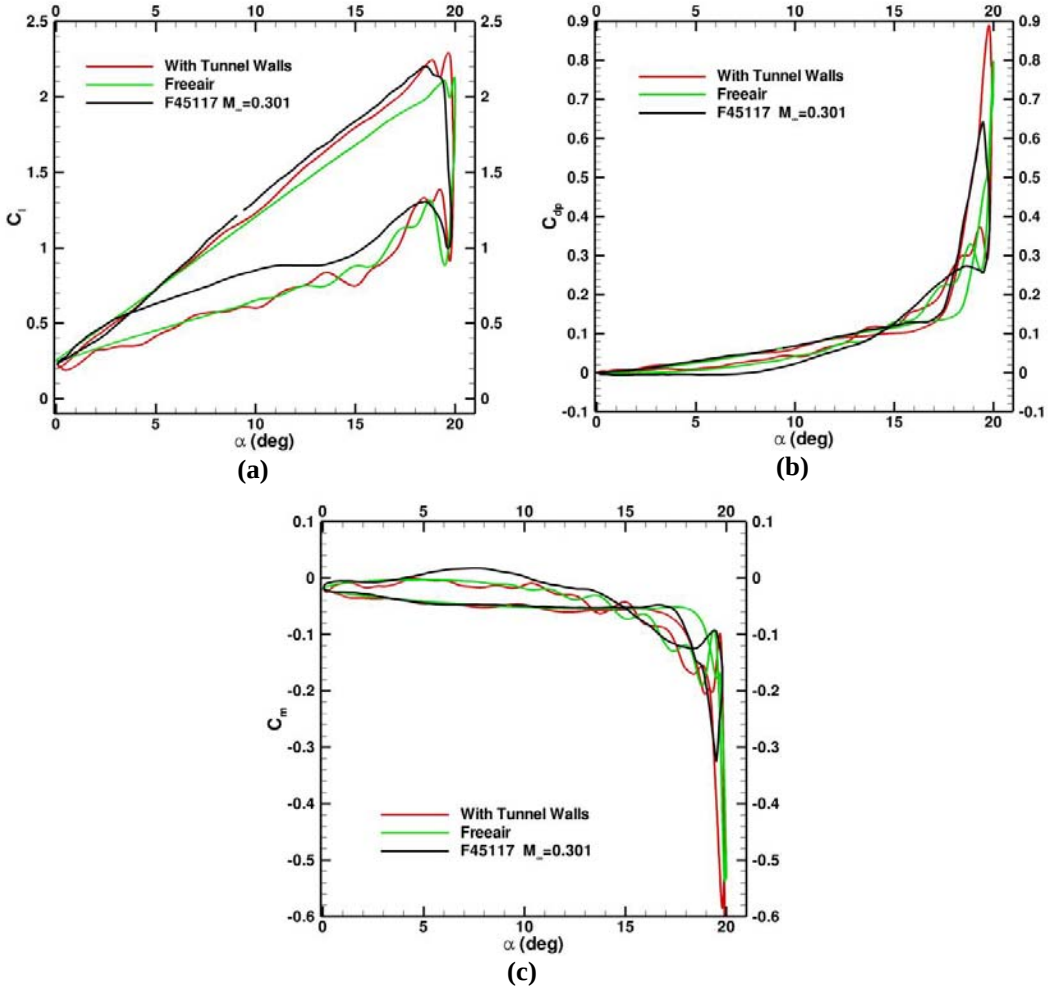

Figure 3 Hysteresis of lift (a), drag (b) and pitching moment (c) coefficients of VR-7 airfoil with and without tunnel walls modeled in computations.

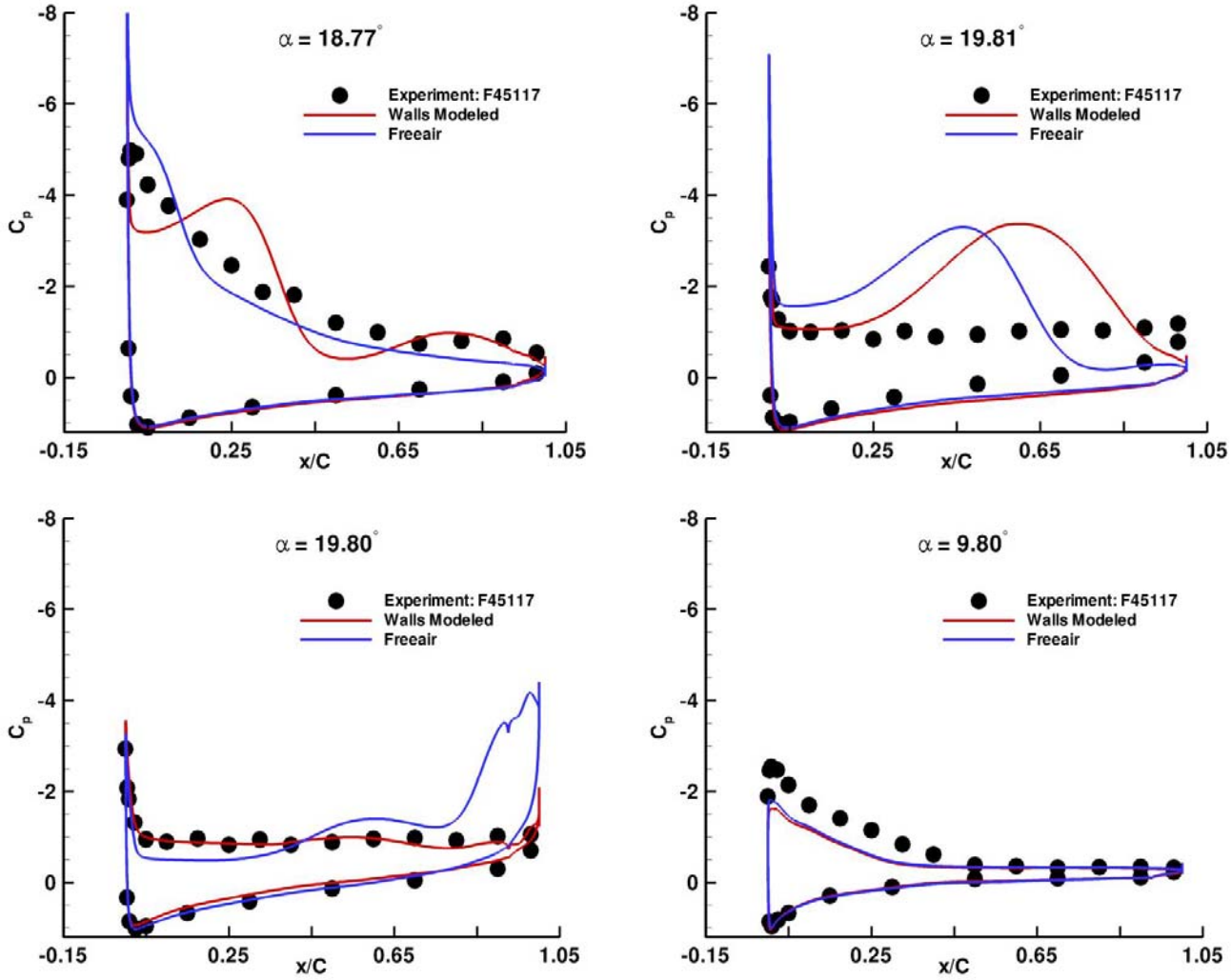

Figure 4 Comparison of computed surface-pressure coefficients of VR-7 airfoils with experimental data.

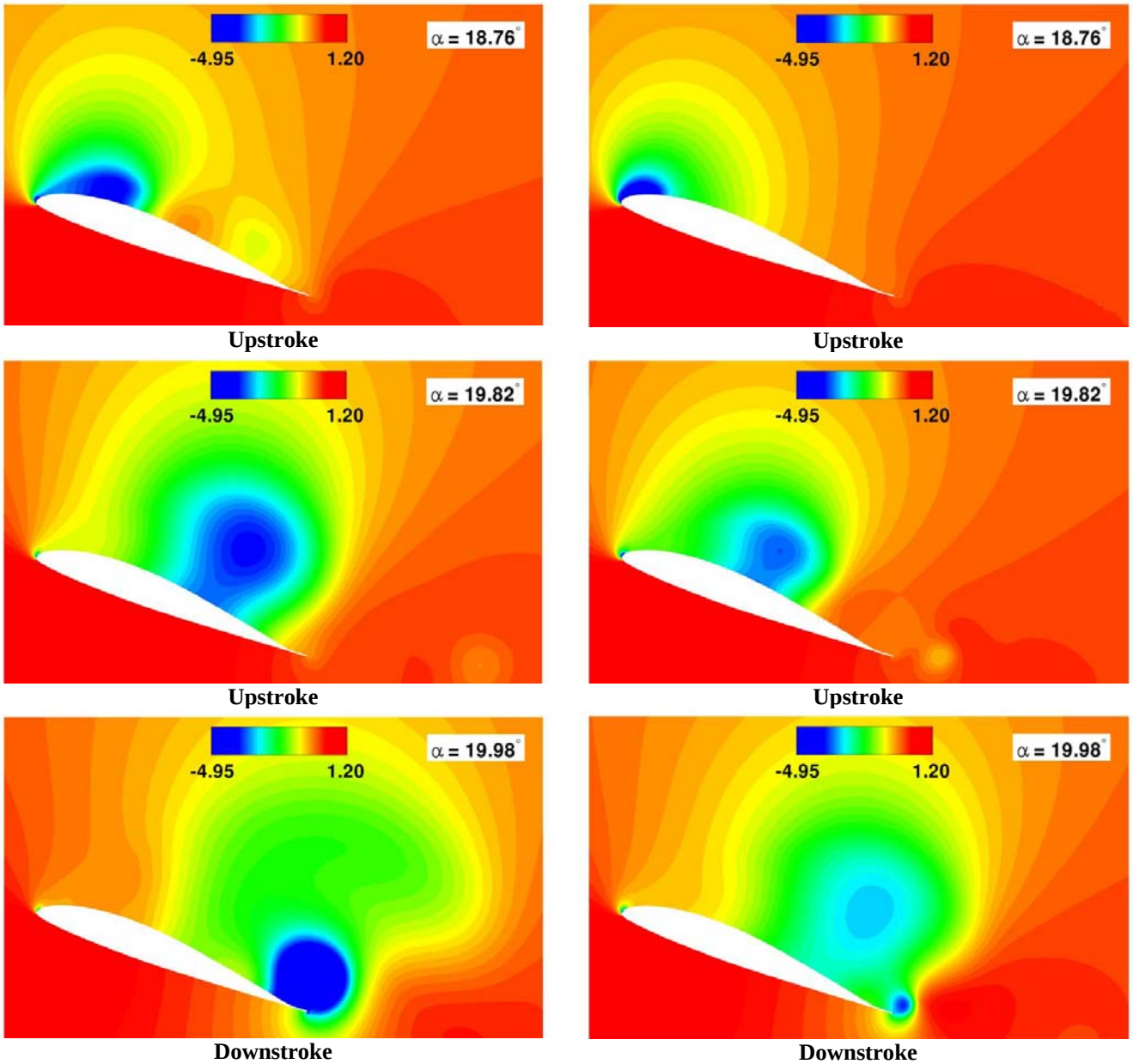

Figure 5 Pressure-coefficient contours of VR-7 airfoils with (left) and without (right) tunnel wall modeled in computations during pitching cycle.

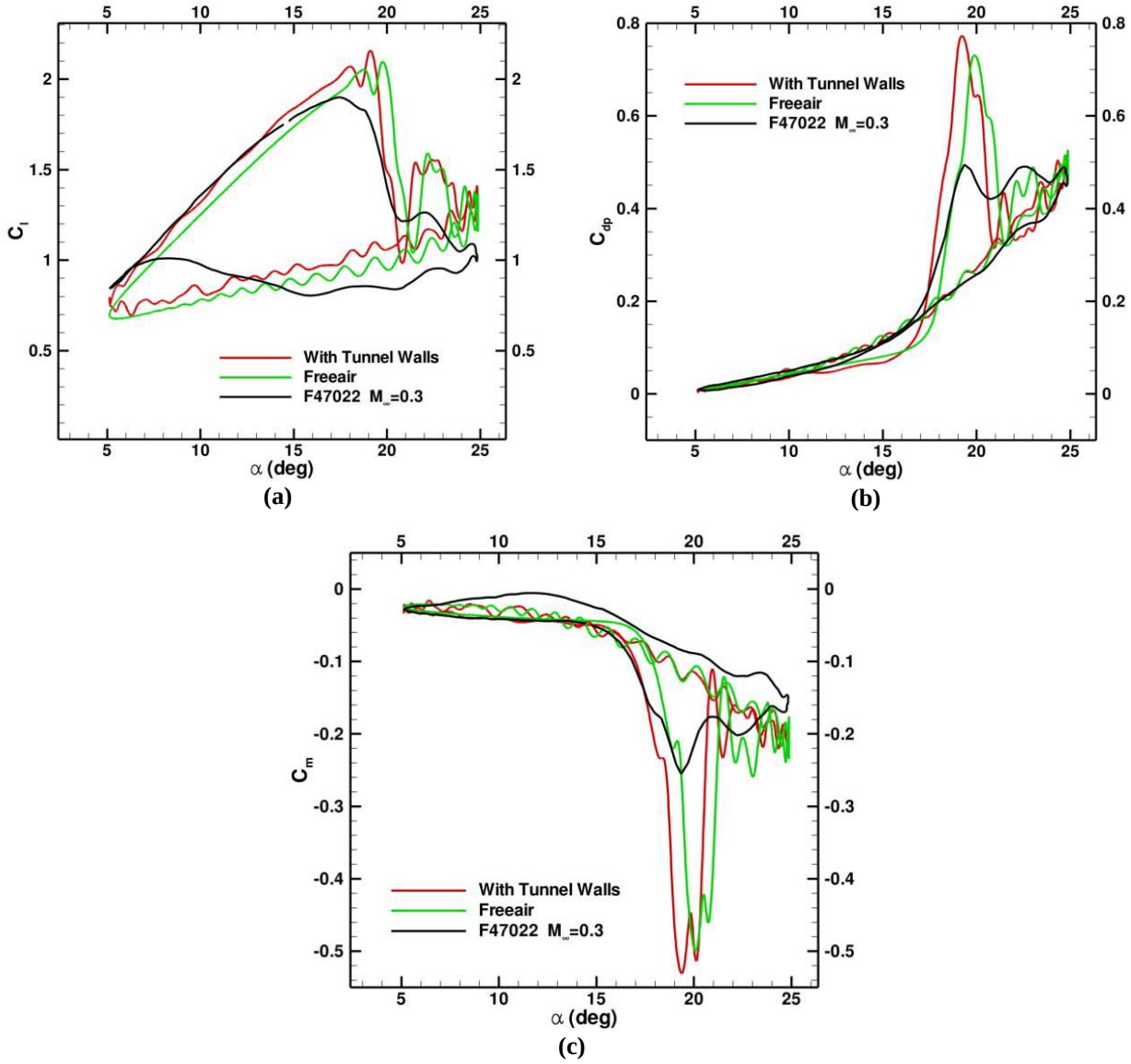

Figure 6 Hysteresis of lift (a), drag (b) and pitching moment (c) coefficients of VR-7 airfoils with and without tunnel walls modeled in computations.

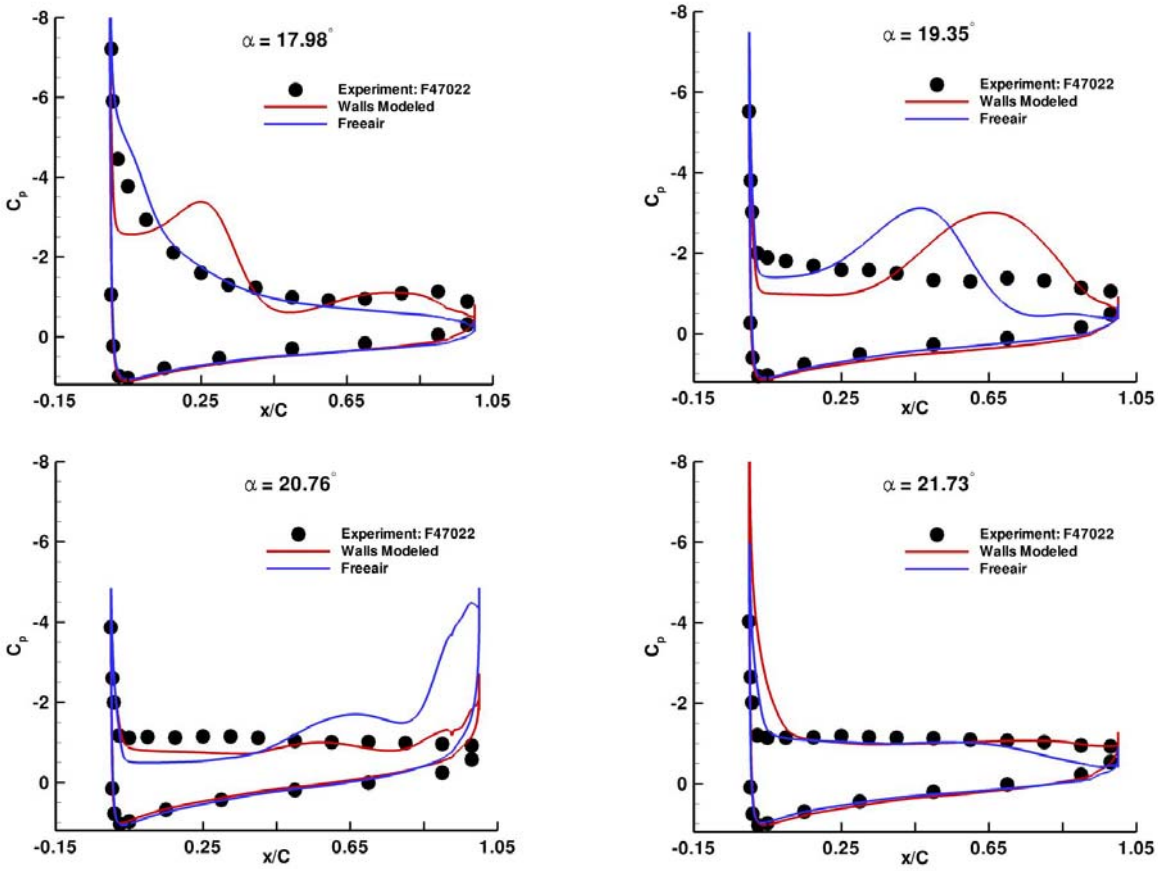

Figure 7 Comparison of surface-pressure coefficient of VR-7 airfoil with experimental data.

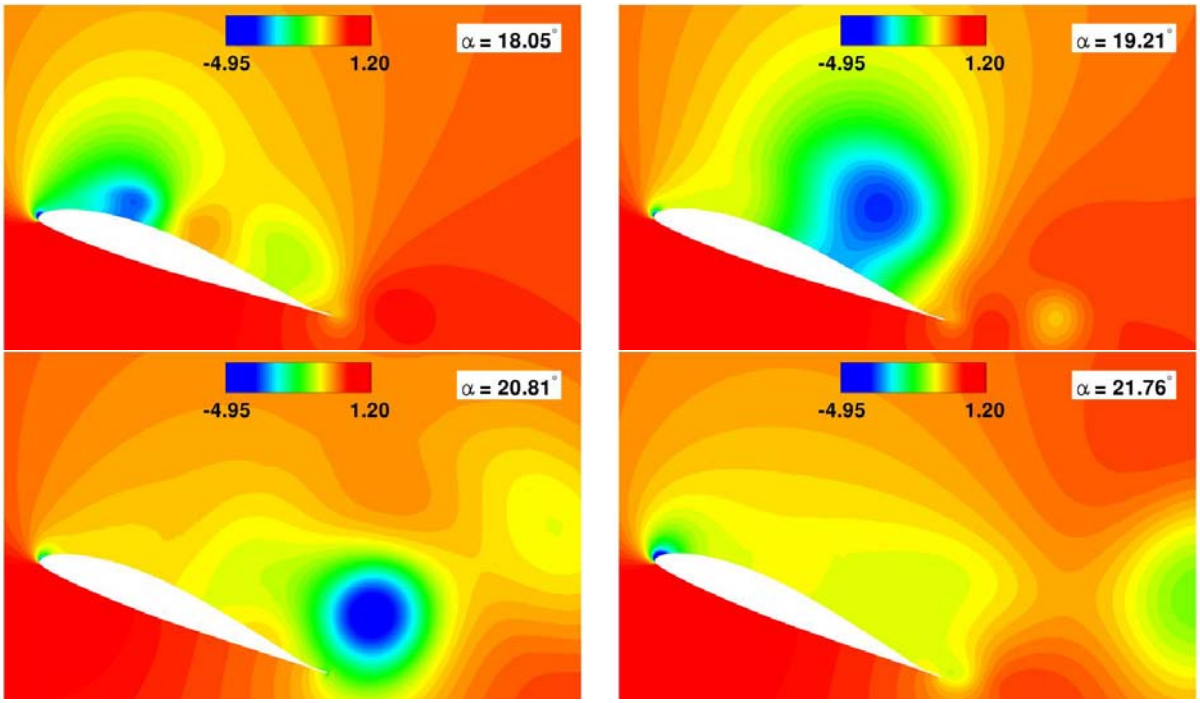

Figure 8 Pressure-coefficient contour of VR-7 airfoils with tunnel wall modeled in computation during pitching oscillation.

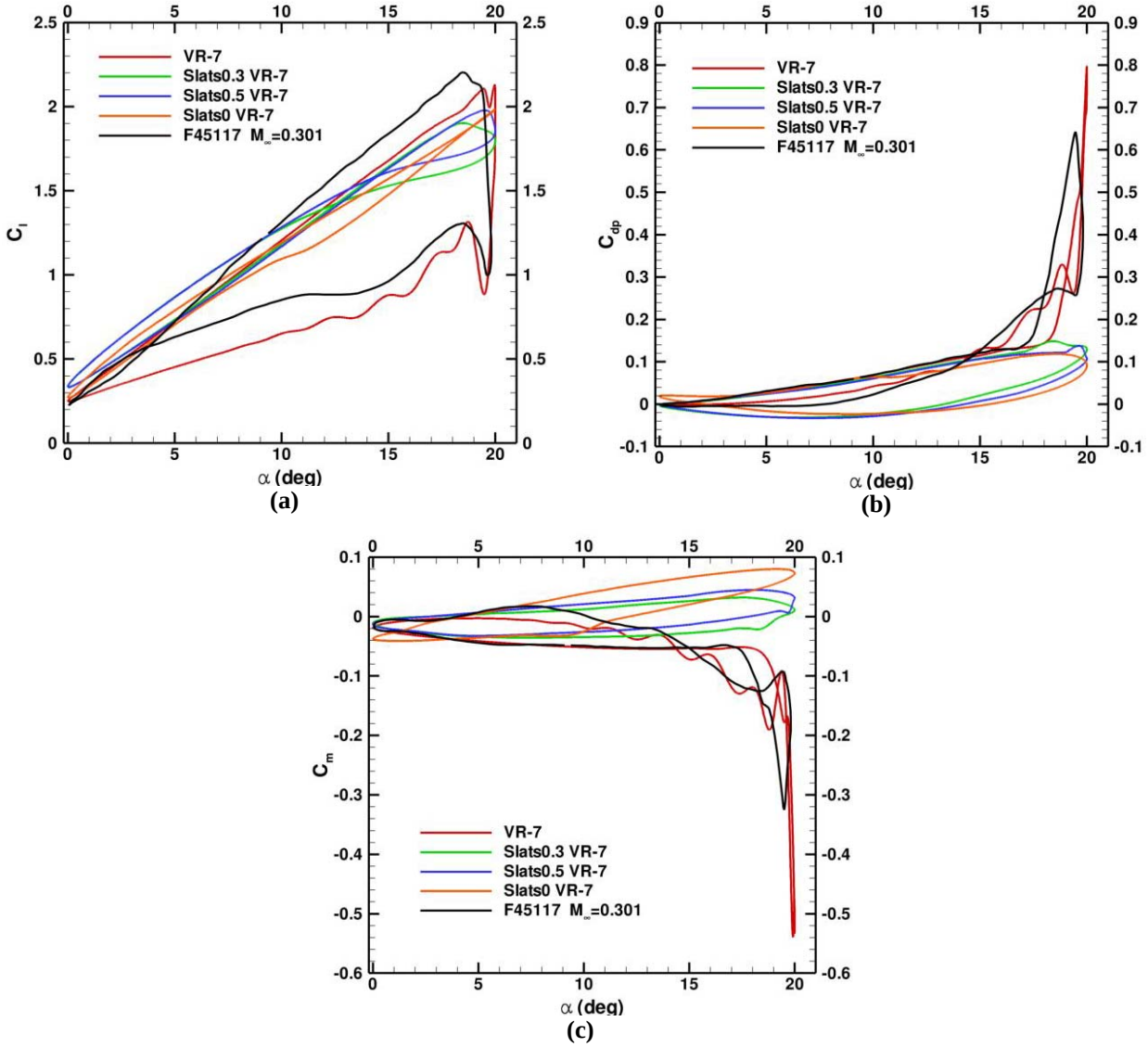

Figure 9 Hysteresis of lift (a), drag (b) and pitching moment (c) coefficients of VR-7, VR-7 with slat airfoils.

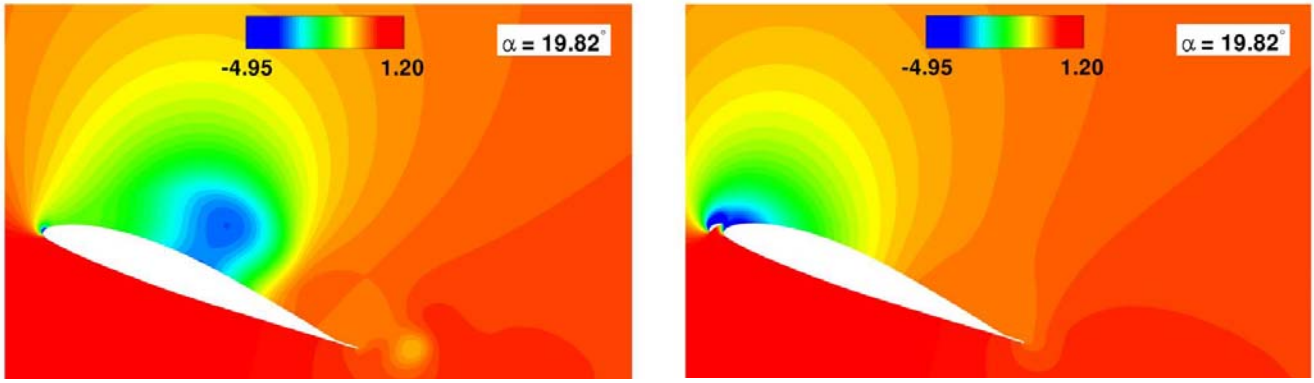

Figure 10 Comparison of pressure-coefficient contours of VR-7 and Slats05-VR-7 airfoils at upstroke pitching oscillation.

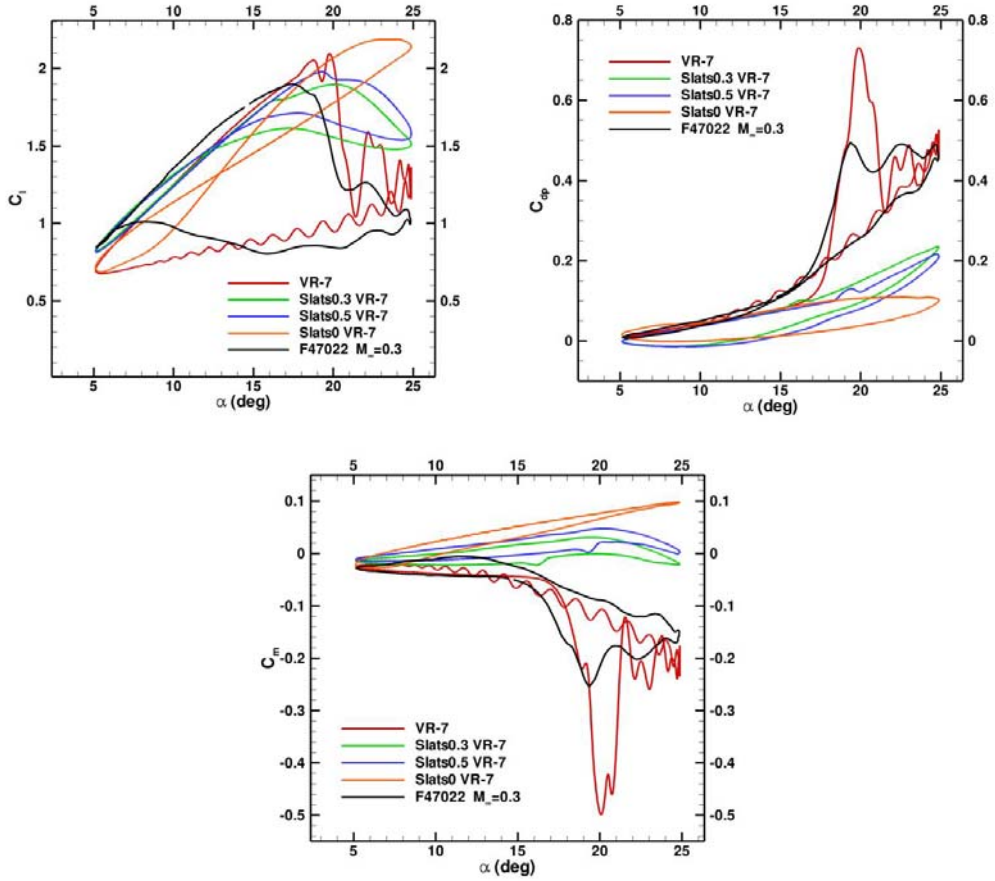

Figure 11 Hysteresis of lift, drag and pitching moment coefficients of VR-7, and three slat VR-7 airfoils.

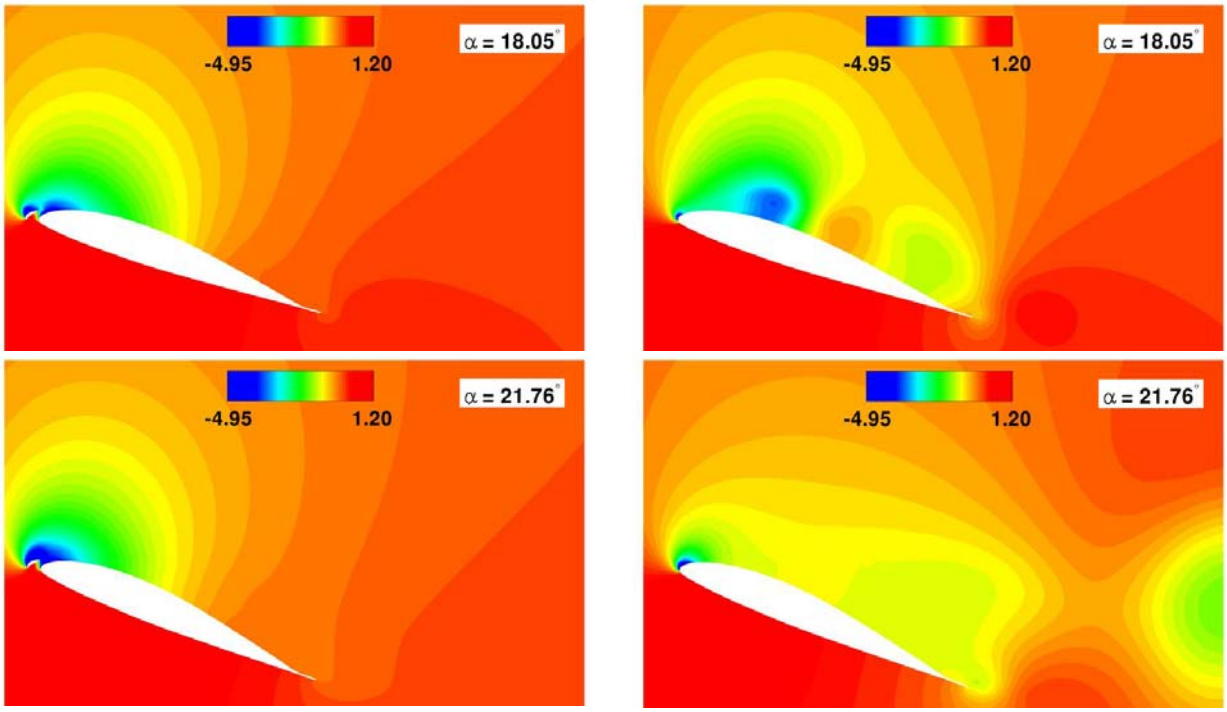

Figure 12 Comparison of pressure-coefficient contours of Slats05-VR-7 (left) and VR-7 (right) airfoils.

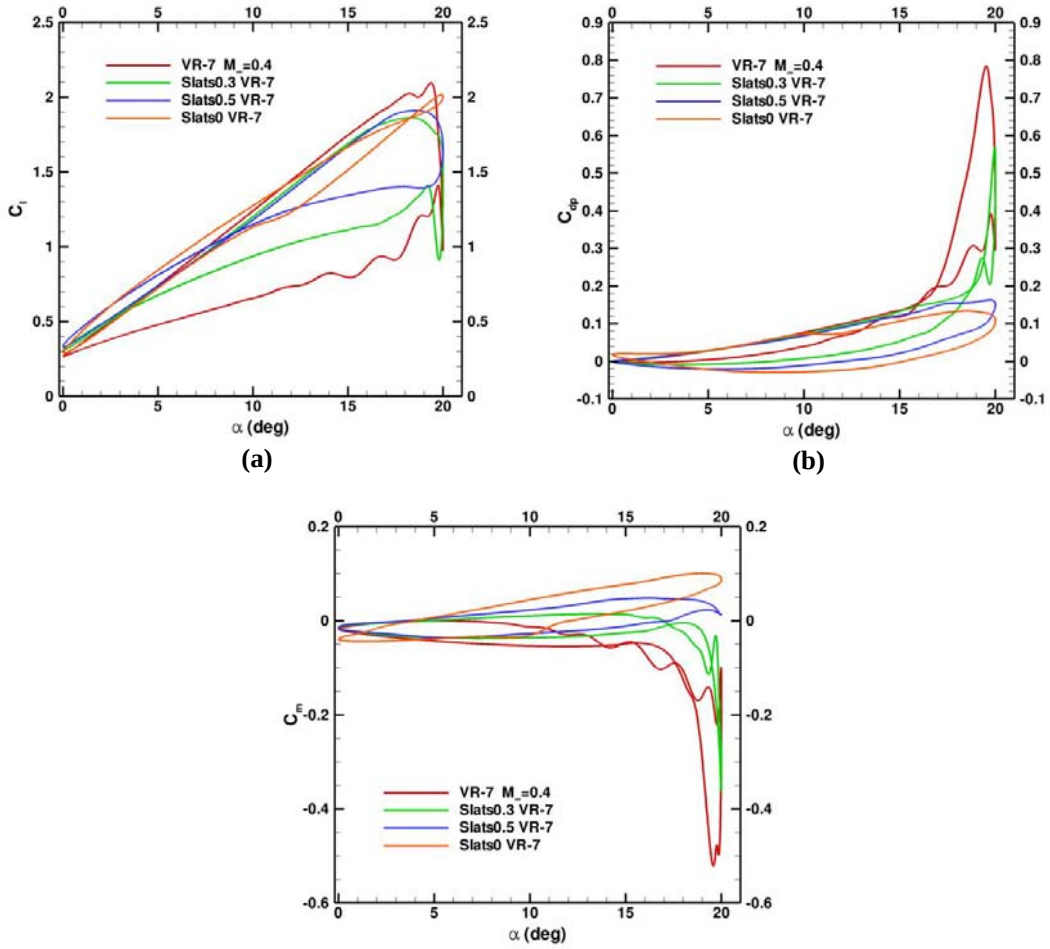

Figure 13 Hysteresis of lift)a), drag (b) and pitching moment (c) coefficients of VR-7 and three slat airfoils.

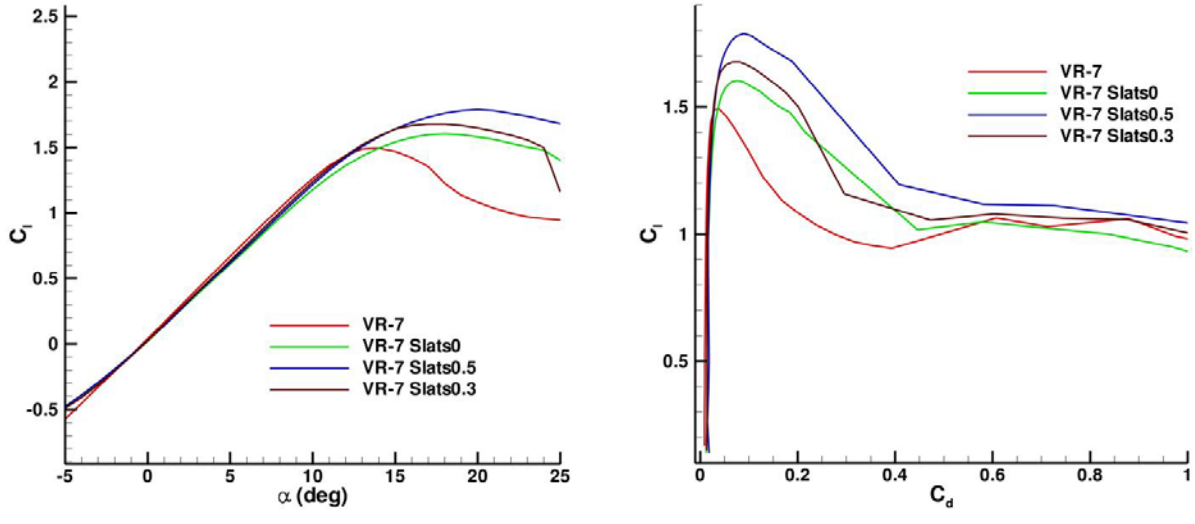

Figure 14 Comparison of lift coefficient (a) and drag polar of VR-7 and three slat airfoils.

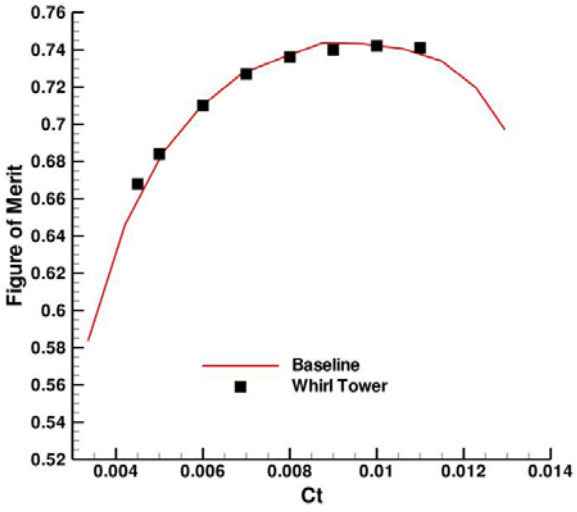

Figure 15 Comparison of hover performance of CH-47D isolated rotor using LSAF with test data.

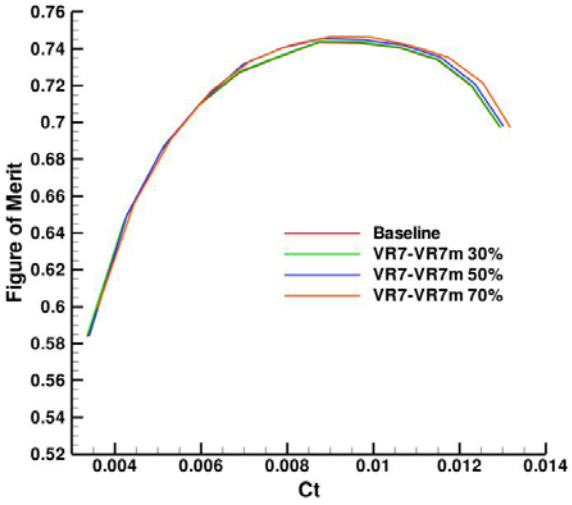

Figure 16 Comparison of LSAF results with VR7m airfoils at three different inboard sections.

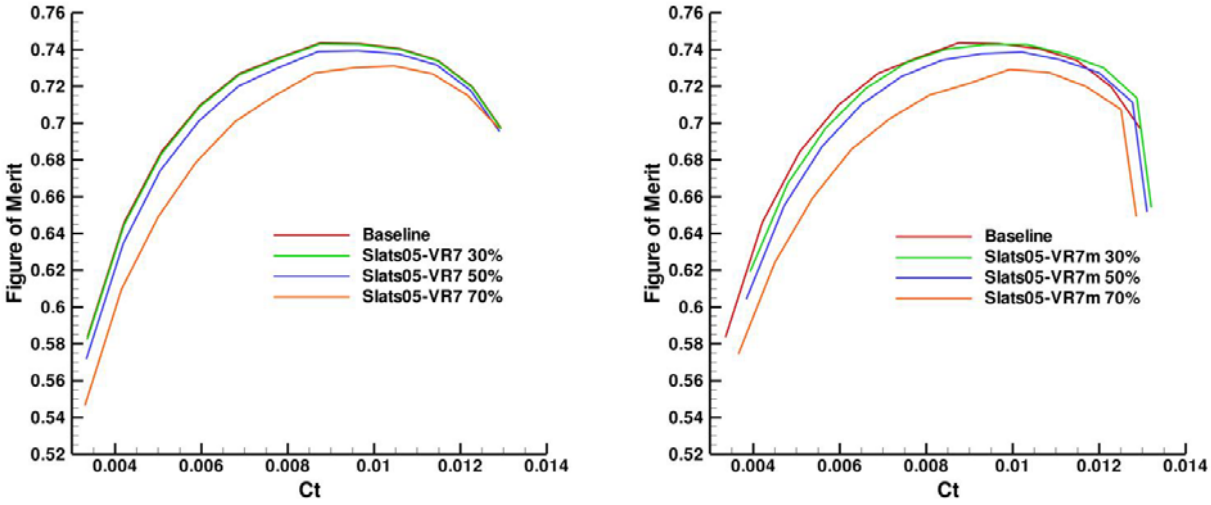

(a) **(b)**

Figure 17 Comparison of LSAF results using Slats0-VR-7 and Slats05-VR7m airfoils at three different inboard sections.